Research Square

Preprints are preliminary reports that have not undergone peer review.
They should not be considered conclusive, used to inform clinical practice,
or referenced by the media as validated information.

A Multiscale Graph Generative Adversarial Network Method for Prediction of Autoclave Curing Temperature Field in CFRP component

Guangqi Qiu
Jiangxi University of Science and Technology
Wenjing Yu
Jiangxi University of Science and Technology
Ning Zhong
Jiangxi University of Science and Technology
Yongqian Xu
yongqian.xu@csu.edu.cn

Central South University
Peng Huang
Jiangxi University of Science and Technology
Yingkui Gu
Jiangxi University of Science and Technology

Article

Keywords: autoclave, curing temperature field, unstructured mesh, graph neural network, fast temperature field prediction

Posted Date: August 14th, 2026

DOI: https://doi.org/10.21203/rs.3.rs-10530248/v1

License: This work is licensed under a Creative Commons Attribution 4.0 International License.
Read Full License

Additional Declarations: No competing interests reported.

A Multiscale Graph Generative Adversarial Network Method for Prediction of Autoclave Curing Temperature Field in CFRP component

Guangqi Qiu,Wenjing Yu, Ning Zhong,Yongqian Xu*, Peng Huang, Yingkui Gu

1.School of Mechanical and Electrical Engineering, Jiangxi University of Science and Technology, Ganzhou, 341000, China

2. Light Alloy Research Institute, Central South University, Changsha 410083, Hunan, China

*Corresponding Author: yongqian.xu@csu.edu.cn

Abstract: During the CFRP component in an autoclave, the spatiotemporal temperature distribution directly affects the forming quality and process efficiency. To address the issues of insufficient multi-scale feature representation and overly smoothed prediction results in existing deep learning surrogate models under unstructured mesh conditions, this paper proposes a rapid prediction method for curing temperature fields based on a multi-scale graph generative adversarial network. Based on the experimentally validated thermo-chemical coupling model of the autoclave curing process, 100 sets of operating condition samples were obtained by sampling around six process parameters, and a spatiotemporal dataset of the whole-process temperature field and degree of cure was constructed. The generator employs two-level CLJP coarsening and graph attention to enhance the representation of temperature-field features at different spatial scales, including global thermal diffusion patterns, local high-gradient features, boundary transition details, and local peak information, while the local graph discriminator alleviates the oversmoothing commonly observed in supervised regression models by imposing realism constraints on hotspot regions and boundary transition zones through k-hop neighborhood-induced subgraphs. The results show that the proposed model outperforms comparative models such as Graph U-Net, Graph U-Net-LSTM, Grid-GAN, and conventional GNN in predicting the cure temperature field, with MAE, RMSE, R^2, and MAX-Error reaching 1.28 ℃, 1.76 ℃, 0.993, and 3.58 ℃, respectively; in full-cycle autoregressive prediction, the model can reducing computation time by approximately 99% compared to traditional CFD simulations. The study results indicate that this method can provide an efficient and reliable surrogate model for rapid evaluation and intelligent control of the curing process in composite material autoclaves.

Keywords: autoclave; curing temperature field; unstructured mesh; graph neural network; fast

temperature field prediction

1. Introduction

Resin-based carbon fiber reinforced composites have been widely used in large load-bearing structures in aerospace due to their high specific strength, high specific stiffness, and strong design flexibility. Autoclave curing, as one of the most commonly used processes in the manufacturing of high-performance composite components, has a temperature field whose spatial and temporal distribution directly affects resin reaction rate, curing uniformity, formation of residual stress, and final dimensional accuracy. With the trend of composite components toward larger sizes and integration, the spatial non-uniformity of flow and heat transfer inside the autoclave becomes more prominent, placing higher demands on the accuracy and efficiency of temperature field prediction during the curing process. Therefore, conducting high-precision and high-efficiency prediction studies on the autoclave curing temperature field is not only a key foundation for improving the forming quality and process stability of composites, but also has significant importance for achieving autoclave process optimization, process monitoring, and intelligent control.

Regarding the numerical modeling of the curing temperature field, existing research has gradually developed from simple heat transfer analysis to high-fidelity modeling that considers flow, heat exchange, curing reactions, and multiphysics coupling. Dolkun et al. [1] studied the impact of the placement of large frame molds on local flow reorganization and temperature distribution. Han et al. [2] analyzed the mechanism by which flow paths and thermal resistance variations around components affect spatial differences in the temperature field. Zhang et al. [3] examined the influence of different mold materials and heat transfer medium combinations on temperature distribution. Sun et al. [4] improved in-tank flow organization and mold temperature uniformity through the optimization of guiding channel structures. Yue et al. [5,6] further enhanced mold heat transfer performance from the perspectives of structural topology optimization and thermo-fluid coupled topology optimization. Xu et al. [7] discussed the effects of process factors such as airflow velocity and heating rate on the evolution of the temperature field. Studies indicate that geometric configuration, material parameters, and process conditions can affect temperature field distribution by changing flow organization and heat transfer characteristics.

Since convective heat transfer plays a dominant role in the formation of the temperature field in the autoclave, Bohne et al. [8] combined CFD and experimental methods to quantitatively analyze the spatial distribution characteristics of the heat transfer coefficient. Weber et al. [9] proposed a method for rapidly generating thermal boundary conditions. Fisher et al. [10] further quantified the impact of heat transfer coefficient non-uniformity on temperature prediction errors. To improve modeling accuracy and engineering applicability, Wang et al. [11] used thermal balance calibration to enhance the accuracy of local heat transfer parameter identification. Zhu et al. [12,13] developed a quasi-transient conjugate heat transfer modeling strategy, which improves computational efficiency while retaining key unsteady features. With deeper research, Yang et al. [14] constructed a fully coupled thermal–fluid–solid analysis framework to describe the interaction between external flow and internal temperature fields. Overall, existing numerical modeling has made considerable progress, but the idealized treatment of the inlet duct structure still leads to boundary condition distortions, further affecting the accuracy of temperature field predictions.

Compared with high-fidelity numerical modeling, research on efficient prediction of the curing temperature field places more emphasis on rapid evaluation under multiple working conditions and online application capabilities. Lin et al. [15] compared various traditional models and pointed out that RBF networks perform well in predicting curing uniformity. Hou et al. [16] established a data-driven mapping model for the prepreg compression molding process. Kyriazi et al. [17] developed a surrogate model for the RTM process. Feng et al. [18] combined finite element methods and data mining to achieve probabilistic prediction of curing deformation in V-shaped components. These methods are highly efficient for rapid screening under multiple conditions, but their modeling targets are mostly scalars or low-dimensional features, and their capability for high-fidelity prediction of the full spatial-temporal distribution of temperature and curing fields remains limited. With the development of deep learning, end-to-end models have gradually become an important direction for rapid prediction of the curing temperature field. Yang et al. [19] utilized deep learning to predict the temperature field of composite materials under the action of a heat source. Zhang et al. [20] combined CNN and LSTM to achieve spatiotemporal temperature field modeling. Wu et al. [21] integrated finite element analysis with deep learning for rapid prediction of temperature fields and degree of cure in large composite blades. To reduce the cost of obtaining high-fidelity samples, Zhang et al. [22] proposed a deep multi-fidelity

surrogate modeling approach. Liu et al. [23] developed a deep learning-based non-contact full-field cure temperature online monitoring method. These studies significantly improved inference speed and also promoted the development from scalar prediction to full-field prediction, but most methods still rely on regular grid representation and large-scale training samples, with limited adaptability to unstructured grids commonly used for complex components.

To alleviate the dependence of purely data-driven methods on the number of samples and to improve physical consistency, physics-constrained learning and neural operator methods have gradually become important directions in this field. Raissi et al. [24] proposed physics-informed neural networks (PINNs), which introduce the residuals of governing equations and boundary conditions into the loss function to achieve unified modeling of both forward and inverse problems. Niaki et al. [25] applied this to the modeling of the curing process in composite material–tool systems. Meng et al. [26] further proposed a physics-constrained neural operator model for coupled thermal-chemical analysis of composite material curing. Meanwhile, DeepONet provides new ideas for field-to-field mapping across different working conditions [27]; Zhao et al. [28] proposed a neural operator framework suitable for different solution domains and parameter conditions. Li et al. [29] proposed physics-informed neural operators (PINO), achieving joint learning of data supervision and physical constraints. Kovachki et al. [30] systematically summarized the role of neural operators in solving partial differential equations. Patel et al. [31] extended physics neural operators for accelerated optimization in autoclave processes. This indicates that efficient prediction research has gradually evolved from traditional machine learning and end-to-end deep learning to a stage of collaborative modeling of data-driven and physics-informed priors.

For complex composite components, the temperature field is usually discretized based on unstructured meshes. Compared with convolution models on regular grids, graph neural networks can propagate features directly on graph structures, making them more suitable for handling unstructured data under complex geometries. Zhou et al. [32] reviewed the applicability of graph neural networks in modeling complex structural data. Würth et al. [33] validated the feasibility of graph networks for solving unsteady, nonlinear physical problems. Grattarola et al. [34] and Li et al. [35] provided methodological foundations for multi-scale representation of graph models from the perspectives of graph pooling and graph coarsening. Overall, graph learning provides a new technical route for predicting temperature fields on unstructured meshes, but there are still

deficiencies in multi-scale representation and local detail preservation.

In summary, the curing temperature field of the autoclave exhibits both non-structural discrete characteristics under complex geometries and significant multi-scale evolution features with local abrupt changes. Single regular grid models, single-scale graph propagation, or purely supervised regression methods are all difficult to simultaneously meet the requirements of geometric adaptability, global–local collaborative modeling, and local structure preservation. Regarding the rapid prediction of the curing temperature field in autoclaves, existing studies have the following three shortcomings:

(1) The physical credibility of the existing data training samples is insufficient. In current rapid prediction studies, most training samples are directly derived from numerical simulation results under idealized boundary conditions, lacking targeted characterization of the autoclave inlet duct structure, local flow organization, and critical heat transfer boundaries. The verification chain between the preliminary model and experiments is also not complete enough. For the curing temperature field of the autoclave, the inlet boundary conditions directly affect the flow field organization and the overall temperature distribution. Even if subsequent rapid prediction models have high fitting accuracy, they may be built on training samples with systematic biases, thereby weakening the reliability of the prediction results and their engineering application value.

(2) Existing data processing methods are insufficiently adaptable to high-dimensional temperature fields on unstructured grids. The curing temperature field in an autoclave is essentially high-dimensional spatiotemporal data defined on an unstructured grid, containing both the spatial topological relationships under complex geometries and information about the full-process evolution. Current processing methods usually rely on resampling onto structured grids or directly modeling on the original high-dimensional field. The former can easily introduce geometric approximation errors and weaken local thermal conduction topology, while the latter incurs higher computational costs and makes it difficult to balance global heat diffusion relationships with local high-gradient details.

(3) Existing fast prediction methods have insufficient ability to represent and constrain regions with high local gradients. The curing temperature field in an autoclave not only exhibits global thermal diffusion characteristics but also contains hotspot regions and gradient transition zones caused by boundary heat transfer and local exothermic reactions. Most existing fast

prediction methods rely on pure supervised regression or global discrimination. Although they can reduce overall error, they are not sensitive enough to the authenticity of local structures, easily causing over-smoothing in hotspot regions and boundary transition zones, and leading to error accumulation during full-process rolling prediction. As a result, the models struggle to simultaneously ensure the preservation of local details and the stability of full-process prediction.

In response to the above issues, this paper constructs a high-reliability data generation method considering the H-slot air duct structure, proposes a data dimensionality reduction method based on graph construction and multi-scale coarsening, as well as a MSCGAN rapid prediction method based on k-hop neighborhood local graph discrimination, thereby achieving high-accuracy rapid prediction of the curing temperature field for unstructured meshes. The specific contributions are as follows:

(1) A high-fidelity data generation method considering the H-channel duct structure was proposed. By using a thermochemical coupled autoclave model with a realistic inlet-boundary representation and a unified multi-condition simulation workflow, the method generated full-cycle temperature-field and degree-of-cure sequences with improved physical fidelity, providing a reliable basis for subsequent rapid prediction.

(2) A data reduction strategy based on KNN graph construction and multiscale CLJP coarsening was proposed for high-dimensional temperature fields on unstructured meshes. This strategy preserved local heat-transfer topology while reducing graph complexity and enlarging the effective receptive field for subsequent learning.

(3) An MSCGAN-based rapid prediction method with k-hop local graph discrimination was developed to enhance both global–local feature representation and local structural realism. The proposed model achieved an MAE of 1.28, an RMSE of 1.76, an $R^2$of 0.993, and a maximum error of 3.58. The autoregressive MAPE remained below 0.81% over the full curing cycle. These results demonstrate the effectiveness of the proposed framework for accurate and efficient prediction of autoclave curing temperature fields.

The structure of this paper is as follows. Section 2 introduces the proposed methods, including high-fidelity data generation strategies, graph construction and multi-scale data dimensionality reduction methods, as well as a local graph discriminator fast prediction framework based on MSCGAN. Section 3 presents the results and discussion, including the

validation of the high-fidelity forward model, graph construction results, fast prediction performance, and ablation analysis of the proposed modules. Section 4 summarizes the main conclusions of this study.

2.The proposed rapid prediction method for temperature field based on MSCGAN

To address the problems of insufficient physical fidelity of training samples, ineffective processing of high-dimensional temperature fields on unstructured meshes, and oversmoothing in local prediction results during rapid prediction of autoclave curing temperature fields, this study proposes an integrated methodology for rapid prediction of curing temperature fields on unstructured meshes. As shown in Fig. 1, the proposed framework consists of three steps: high-fidelity data generation, graph construction and multiscale data reduction, and MSCGAN-based rapid prediction with local graph discrimination. Compared with existing methods, the proposed approach produces more reliable training samples through high-fidelity coupled simulation, achieves effective representation and complexity reduction of unstructured temperature fields through graph construction and multiscale coarsening, and enhances realism constraints in hotspot regions and boundary transition zones through local graph discrimination, thereby improving prediction accuracy and full-cycle stability.

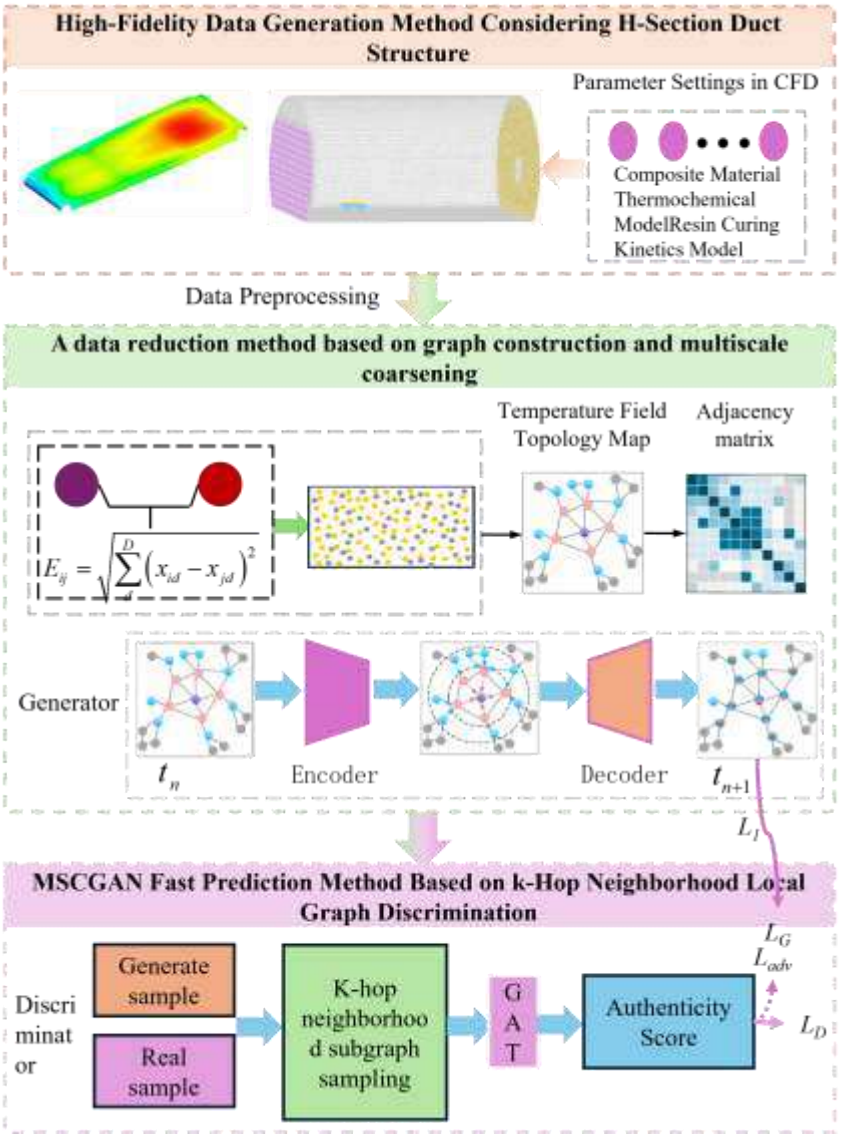


Figure 1 Overview of the MSCGAN method for rapid prediction of curing temperature fields in unstructured meshes

2.1 High-Fidelity data generation method

To address the problem in existing rapid prediction studies where training samples mostly come directly from idealized numerical results and the physical credibility of the samples is insufficient, this paper proposes a high-fidelity data generation method considering the H-channel wind tunnel structure. Based on the previously established and experimentally validated thermo-chemical coupling model of the autoclave, this method constructs unified full-process temperature field and degree-of-cure time-series samples through geometric modeling, meshing, flow–heat–cure reaction coupled simulation, and multi-condition parameter sampling. Compared with

directly using idealized numerical results, this method improves the physical credibility of the samples through more realistic inlet boundary representation and high-fidelity simulation procedures. Figure 2 shows the corresponding workflow of data generation and dataset construction.

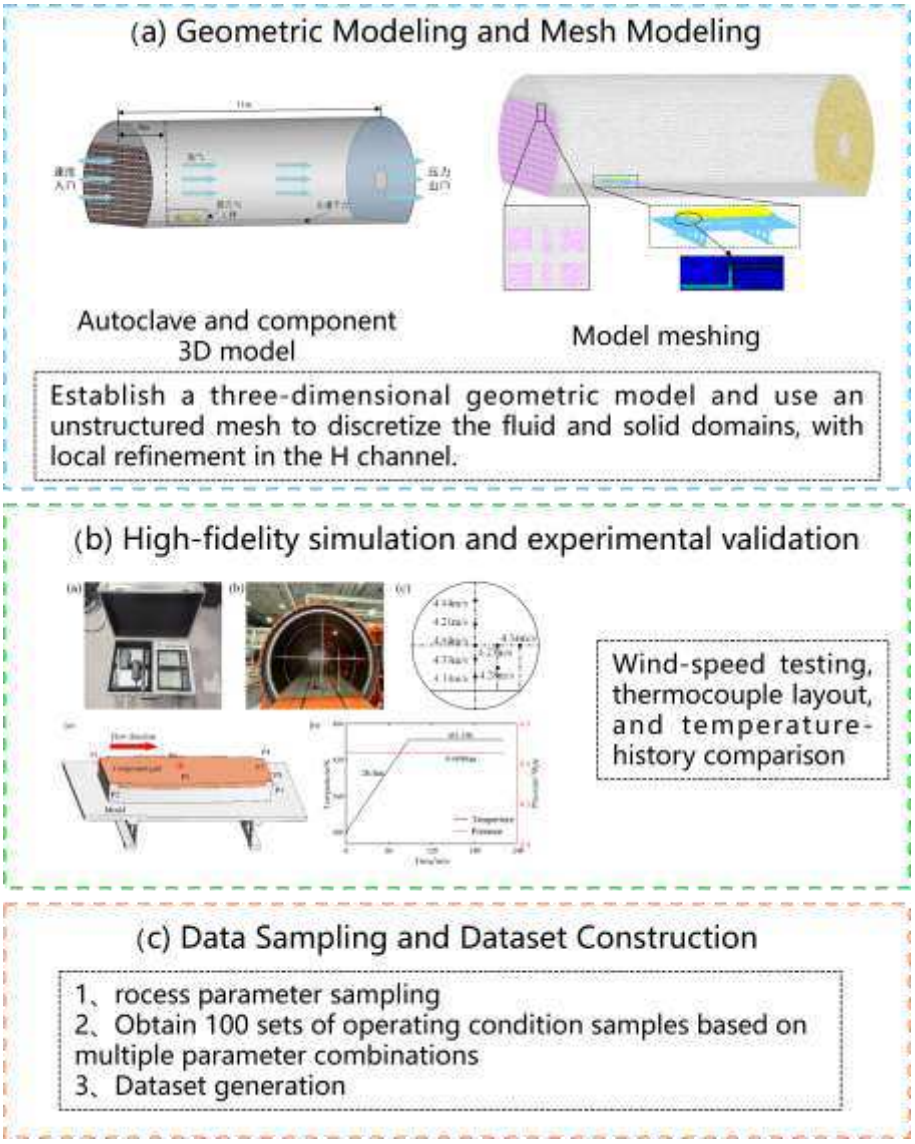


Figure 2 Data sources and dataset construction framework for fast prediction model training

Regarding the issues of complex geometry, sensitive boundary conditions, and significant local heat transfer differences in the autoclave curing process, this paper, based on the previously established autoclave process system, constructs a three-dimensional model that includes the autoclave cavity, inlet duct, mold, composite components, and supporting structures, while retaining the H-slot duct structure to describe the impact of inlet air organization on flow field

distribution and local heat transfer conditions. During the discretization process, unstructured meshes are used to uniformly divide the fluid and solid domains, with local refinement in the inlet area, fluid-solid coupling interfaces, and near components to ensure solution accuracy and computational efficiency.

To address the issue that, during the autoclave curing process, the coupling of fluid flow, heat transfer, and curing reactions makes it difficult for a single physical field model to fully characterize the temperature evolution pattern, this paper introduces a unified solution framework for fluid flow, heat transfer, and resin curing reactions in the pre-model. During simulation, the autoclave process parameters are used as input, and the full-process temperature field and degree of cure field sequences are output using a transient time-stepping approach, thereby forming a unified sample base.

To address the problem that a single operating condition sample is insufficient to support the rapid prediction model in learning the variation patterns of process parameters, based on a high-reliability pre-model, this paper conducts multi-condition sampling around the key process parameters of the autoclave curing process. The sampled parameters include the first-stage curing time, first-stage curing temperature, first-stage heating rate, second-stage curing time, second-stage curing temperature, and second-stage heating rate, totaling six process parameters. By combining these parameters, 100 sets of different operating condition samples were generated, and a transient simulation with a time step of 10 s was conducted for a duration of 13,200 s for each condition to obtain the temperature field and degree of cure field sequences throughout the entire process. Sampling around the six process parameters resulted in 100 sets of different condition samples. To ensure the stability of the model training process and the reproducibility of the evaluation results, the simulation data need to be processed for time step alignment, feature normalization, supervised sample construction, and dataset division before network modeling.

Since each group's working conditions use the same time step and total duration, the time indices are first uniformly aligned. To address the problem of large differences in the dimensions and value ranges of continuous variables such as temperature and degree of cure, the Min-Max normalization method is used to map features to the [0,1] range. For any variable, its normalized form is:

$$\tilde{x} = \frac{x - x_{\min}}{x_{\max} - x_{\min} + \varepsilon} \tag{1}$$

In the formula: $x_{\max}$ and $x_{\min}$ are obtained from statistics of the training set; ε is a very small constant to prevent the denominator from being 0, and this paper takes $\varepsilon = 1e-8$. The test set strictly reuses the statistics of the training set for same-scale transformation to ensure the fairness and comparability of the evaluation results. Finally, a supervised dataset suitable for MSCGAN training and validation is formed.

2.2 A data dimensionality reduction method based on KNN graph construction and multi-scale coarsening

To address the problem that the autoclave curing temperature field is defined on an unstructured mesh, with high-dimensional original field data that is difficult to directly input into deep learning models, this paper proposes a graph construction and multi-scale complexity reduction method. First, the unstructured mesh temperature field is converted into graph-structured data, allowing local heat conduction relationships to be explicitly expressed in a node–edge form; subsequently, through local sparse graph construction and hierarchical graph coarsening, the original high-dimensional graph representation is compressed into multi-scale representations suitable for graph network learning, thereby reducing modeling complexity while preserving geometric topological information and local heat conduction features as much as possible. Compared with regular grid resampling or direct full-graph propagation at a single scale, this method is more suitable for handling autoclave curing temperature fields under complex component conditions and also provides reasonable inputs for the subsequent multi-scale encoding–decoding and local subgraph discrimination in MSCGAN. Figure 3 shows the MSCGAN generator structure and the graph message passing mechanism diagram.

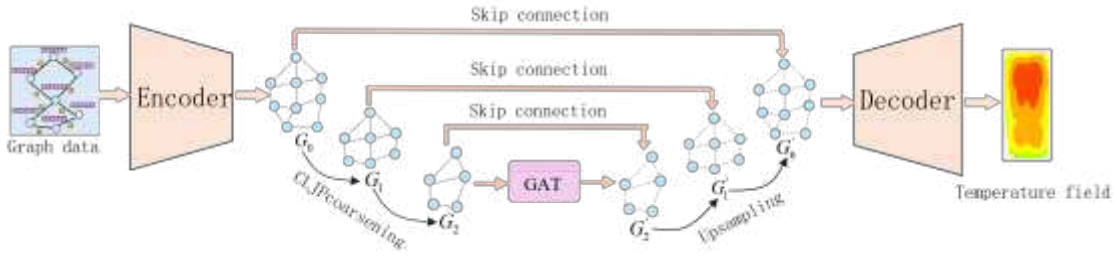


Figure 3 Multiscale graph generator and graph message-passing mechanism in the MSCGAN framework

To address the problem that the structured grid method requires interpolation or resampling of unstructured field data and easily introduces geometric approximation errors, this paper represents the temperature field as graph-structured data, where the graph is represented as:

$$G = (V, E) \tag{2}$$

In the formula: $V = \{v_1, v_2, \ldots, v_N\}$ is the set of nodes, E is the set of edges, N represents spatial discrete nodes.

The graph nodes are defined by the mesh-based spatial discretization of the component temperature field and remain fixed during curing. Each node feature combines local physical variables, shared process information, and spatial coordinates, thereby encoding both local thermal states and location-dependent heat-transfer effects.

The feature vector of the node at the time step is defined as:

$$X_i^t = \left[T_i^t, \alpha_i^t, \dot{T}^n, T_{\text{proc}}^t, x_i, y_i, z_i \right]^T \tag{3}$$

Node features include instantaneous temperature, degree of cure, heating rate, process set temperature, and spatial coordinates, whereas edges represent local heat-transfer relationships. A KNN-based sparse topology is adopted to balance computational efficiency and local structural preservation, and the graph connectivity is kept fixed throughout curing.

Let the spatial position of the node in the autoclave coordinate system be $P_i = (x_i, y_i, z_i)$. For any node v_i , calculate its Euclidean distance to the remaining nodes:

$$d_{ij} = \| P_i - P_j \|_2 \tag{4}$$

The proposed method directly models the temperature field on unstructured meshes as a graph, avoiding interpolation errors and preserving local heat-transfer topology.

To capture both global diffusion and local high-gradient details, the generator employs a graph encoder–decoder with two-level CLJP coarsening, a bottleneck GAT layer, and skip connections.

The encoder progressively builds a hierarchical graph sequence through CLJP coarsening, yielding a coarse-scale graph and a fine-to-coarse mapping, which is described by the prolongation operator below:

$$P^{(l)} \in R^{N_l \times N_{l+1}} \tag{5}$$

The coarsening mapping relies only on the mesh topology and edge connections, and $P^{(l)}$ can be constructed offline before training and shared across all time steps. After completing message passing at the same scale on the encoding side, a restriction operation is used to aggregate fine-scale representations to the coarse scale:

$$H^{(l+1)} = (P^{(l)})^{\top} \bar{H}^{(l)} \tag{6}$$

In the formula: $\bar{H}^{(l)}$ represents the node representation of the l-th layer after message passing updates before coarsening; the decoder uses the prolongation operation to map the coarse-scale representation back to the fine-scale node space, which can be written as:

$$\tilde{H}^{(l)} = P^{(l)} H_{\text{dec}}^{(l+1)} \tag{7}$$

where $H_{\text{dec}}^{(l+1)}$ denotes the node features at the $(l+1)th$ decoder layer.

The coarse-scale adjacency matrix is constructed using a Galerkin projection:

$$A^{(l+1)} = (P^{(l)})^{\top} A^{(l)} P^{(l)} \tag{8}$$

This procedure yields a hierarchical graph sequence for bottleneck feature extraction and decoder-side reconstruction. At each scale, feature learning is performed by a Graph Attention Network (GAT), which adaptively weights neighborhood information to emphasize prediction-relevant nodes, as shown in Fig. 3.

A shared linear transformation is first applied to the node representations to project them into the attention space:

$$\tilde{h}_i^{(l,s)} = W^{(l,s)} h_i^{(l,s)} \tag{9}$$

where $W^{(l,s)} \in R^{d' \times d}$ is a learnable parameter matrix and d' denotes the projected feature dimension.

For each adjacent node pair $(i, j)\,(j \in \mathrm{N}(i))$, the concatenated feature vector is used to compute the unnormalized attention coefficient:

$$e_{ij}^{(l,s)} = \mathrm{LeakyReLU}\left(a^{(l,s)\top} \left[\tilde{h}_i^{(l,s)} \,\|\, \tilde{h}_j^{(l,s)}\right]\right) \tag{10}$$

where $a^{(l,s)} \in R^{2d'}$ is a learnable vector, $[\cdot \| \cdot]$ denotes vector concatenation, and LeakyReLU introduces nonlinearity while avoiding complete gradient vanishing in the negative half-axis.

A softmax normalization is then applied over the neighborhood of node i to obtain the attention weight of neighbor j with respect to node i:

$$\alpha_{ij}^{(l,s)} = \frac{\exp\left(e_{ij}^{(l,s)}\right)}{\sum_{k\in \mathrm{N}(i)} \exp\left(e_{ik}^{(l,s)}\right)}. \tag{11}$$

where $\alpha_{ij}^{(l,s)}$ measures the importance of neighbor j in updating the feature of node i.

The node representation is updated by a weighted sum of projected neighborhood features:

$$h_i^{(l,s+1)} = \sigma\left(\sum_{j\in \mathrm{N}(i)} \alpha_{ij}^{(l,s)} \tilde{h}_j^{(l,s)}\right) \tag{12}$$

where $\sigma(\cdot)$ denotes a nonlinear activation function.

To enhance representation capacity and improve training stability, multi-head attention is adopted.Calculate $\alpha_{ij}^{(l,s)}$ and $\tilde{h}_{j,k}^{(l,s)}$ for each head respectively, and concatenate the outputs of each head to obtain the final updated result:

$$h_i^{(l,s+1)} = \Big\|_{k=1}^{K} \sigma\left(\sum_{j\in \mathrm{N}(i)} \alpha_{ij,k}^{(l,s)} \tilde{h}_{j,k}^{(l,s)}\right) \tag{13}$$

where K is the number of attention heads and $\|$ denotes concatenation.

This mechanism enables parallel modeling of neighborhood dependencies in multiple subspaces, improving the representation of spatially non-uniform features.

During upsampling, the fine–coarse mapping progressively restores fine-scale resolution and propagates coarse-scale global information back to the original node space. Skip connections further compensate for coarsening-induced detail loss by directly fusing encoder features with decoder features at the same scale.

The fused decoder representation is defined as:

$$H_{\mathrm{dec}}^{(l)} = \mathrm{Fuse}(\tilde{H}^{(l)}, \bar{H}^{(l)}) \tag{14}$$

The fusion operator uses concatenation followed by a linear mapping to align feature dimensions and mix information:

$$\mathrm{Fuse}(A, B) = W_f[A \,\square\, B] + b_f \tag{15}$$

where $[\cdot\,\square\,\cdot]$ denotes channel-wise concatenation, and W_f and b_f are learnable parameters. After fusion, additional GAT layers refine the features at the same scale, allowing the decoder to recover resolution and restore encoder-preserved details. At the finest scale, an output head maps the node features to the temperature prediction at the next time step:

$$\hat{T}_{l+1} = \psi_{\text{out}}\left(H_{\text{dec}}^{(0)}\right) \tag{16}$$

where $\psi_{\text{out}}(\cdot)$ is the output layer,maps the node embedding to the scalar physical quantity of temperature.

2.3 MSCGAN fast prediction method based on k-Hop neighborhood local graph discrimination

To address the insufficient capability of existing rapid prediction methods in representing and constraining local high-gradient regions, this study proposes an MSCGAN-based rapid prediction method with local graph discrimination. The method takes the hierarchical graph representation as input, uses a multiscale graph generator to learn the global–local collaborative features of the temperature field, and employs a local graph discriminator to impose realism constraints on hotspot regions and boundary transition zones. The discriminator concatenates the conditional graph with the real or generated graph at the next time step, samples k-hop neighborhood-induced subgraphs around selected center nodes, and outputs dense local realism scores through a GAT-based backbone. In this way, the model can better preserve local structures while maintaining global predictive consistency. Compared with structured-grid convolutional networks, conventional single-scale graph networks, and purely supervised regression methods, the proposed approach is better suited to unstructured-mesh inputs, provides stronger multiscale feature representation, and offers more targeted local structural constraints, thereby alleviating oversmoothing and improving full-cycle prediction stability.Figure 4 is a schematic diagram of the local graph discriminator structure based on local subgraph sampling.

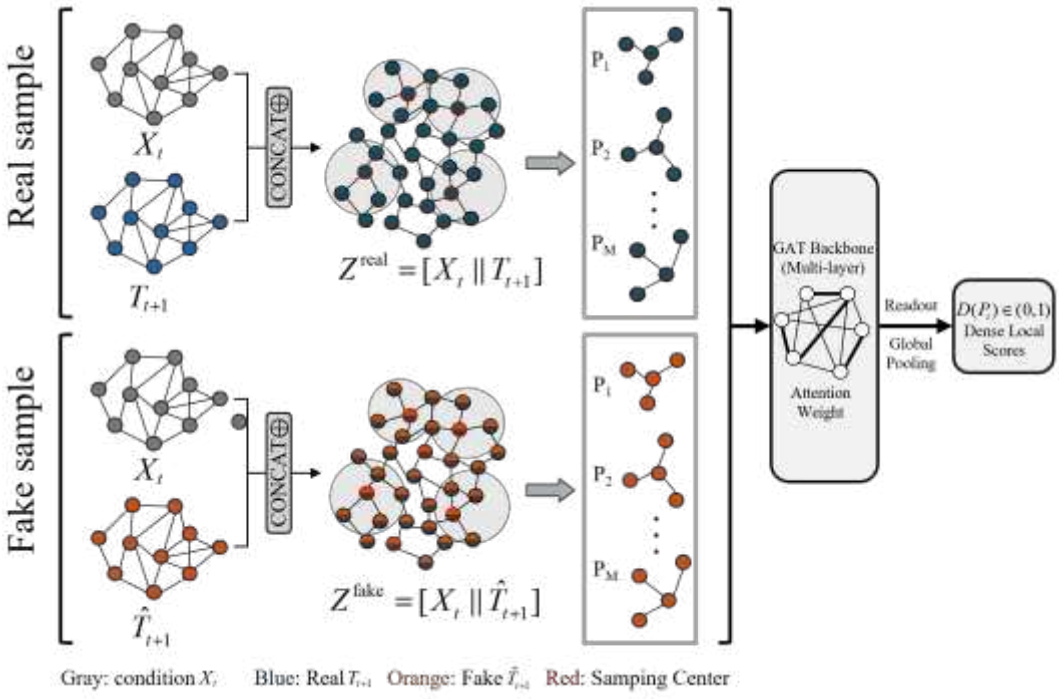


Figure 4 Local graph discriminator based on k-hop neighborhood-induced subgraph sampling

To address the problems of over-smoothing in purely supervised regression and the insensitivity of global discriminators to local structural distortions, this paper constructs a local graph discriminator based on k-hop neighborhood-induced subgraphs, extending the idea of PatchGAN's local discrimination to graph-structured data, constraining the spatial authenticity of hotspot areas and boundary transition zones, thereby improving the ability to preserve local structures in prediction results.

Construct a node k-hop neighborhood induced subgraph discriminator, applying authenticity constraints block by block to local patches, in order to improve the structure preservation capability near hotspot areas, boundary transition zones, and local peaks. Its structural diagram is shown in Figure 4.

During training, the generator outputs the predicted temperature at the next time step $\hat{T}_{t+1}$， ， and the ground-truth label is denoted by T_{t+1}.Specifically, the discriminator takes node-wise concatenated features as input. For real samples, the input is constructed as:

$$Z^{\text{real}} = [X_t \, \square \, T_{t+1}], \tag{17}$$

For generated samples, the input is constructed as:

$$Z^{\text{fake}} = [X_t \,\|\, \hat{T}_{t+1}], \tag{18}$$

where $[\cdot][\cdot]$ denotes feature concatenation and X_t represents the node features at time t.

In this study, a graph-domain patch is defined as the induced k-hop neighborhood subgraph of a node. For any center node v_i, the induced subgraph is defined as:

$$P_i = G[N_k(i)], \tag{19}$$

During training, central nodes are sampled to construct local discriminative subgraphs, enabling the discriminator to focus on local thermal neighborhoods. Combined with supervised regression loss, this node-level adversarial constraint better preserves local realism and detail consistency. Single-step samples are used for stable training, while autoregressive rolling prediction is used in validation to assess long-horizon stability.

The L1 loss is adopted as the main supervised term, and the prediction error is averaged over all nodes:

$$\mathrm{L}_{\mathrm{L1}} = \frac{1}{N}\sum_{i=1}^{N}\left|\hat{T}_i^{t+1} - T_i^{t+1}\right| \tag{20}$$

Compared with L2, the L1 loss is more robust to local peaks and high-gradient regions.

The discriminator adopts a conditional discrimination scheme. Using X^t as the condition, node-level concatenated features are constructed for real and generated samples, respectively:

$$Z^{\text{real}} = [X^t \,\|\, T^{t+1}], \quad Z^{\text{fake}} = [X^t \,\|\, \hat{T}^{t+1}] \tag{21}$$

where $\hat{T}^{t+1} = [\hat{T}_1^{t+1}, \ldots, \hat{T}_N^{t+1}]^{\cdot}$ and $[\cdot][\cdot]$ denotes concatenation along the feature dimension.

he discriminator loss is defined using binary cross-entropy (BCE):

$$\mathrm{L}_D = -\frac{1}{M}\sum_{m=1}^{M}\Big[\log D(P_m, Z^{\text{real}}) + \log\big(1 - D(P_m, Z^{\text{fake}})\big)\Big], \tag{22}$$

The adversarial loss of the generator encourages generated samples to be classified as real:

$$\mathrm{L}_{\text{adv}} = -\frac{1}{M}\sum_{m=1}^{M}\log D(P_m, Z^{\text{fake}}). \tag{23}$$

The patch-level BCE constraint provides dense local adversarial signals on the graph, enabling the generator to match both nodal values and local structural distributions.

The generator is optimized jointly, with the supervised term as the primary objective and the adversarial term as an auxiliary objective:

$$L_G = L_{L1} + \lambda_{adv} L_{adv} \tag{24}$$

Training is performed using single-step prediction sample pairs (X^t, T^{t+1}). This strategy stabilizes the supervised target distribution, facilitates adversarial convergence, and improves one-step prediction accuracy.

3. Results analysis and Discussion

3.1 Temperature field during the autoclave curing process

The operating parameters and dataset configuration used in this study are summarized in Table 1. Based on the high-fidelity forward model, six key process parameters were sampled to generate 100 operating conditions. Transient simulations were then performed with a time step of 10 s over a total duration of 13,200 s to obtain full-cycle temperature-field and degree-of-cure sequences for subsequent training and validation.

Table 1 Operating Parameters and Dataset Construction

Category	Parameter	Value or Description
Process parameters	First stage heating rate, first stage holding temperature, first stage holding time	Sample variable
Process parameters	Second stage heating rate, second stage holding temperature, second stage holding time	Sample variable
Sample size	Number of operating conditions	100 sets
Time discretization	Time Step	10 s
Time discretization	Total Duration	13200 s
Output variable	Temperature Field and Degree of Cure Field	Full-process transient sequence

The temperature-field distributions obtained with and without the H-duct structure are presented in Fig. 5.

The results at 45 min show that the process is still dominated by forced convection, while internal heat conduction has not yet become significant. In the H-duct case, the isotherms exhibit a more symmetric double-peak pattern, indicating that the inlet flow is redistributed more uniformly over the component surface. By contrast, the model without the H-duct already shows

a stronger asymmetry, with a pronounced hot region forming on the windward side and a lower-temperature zone persisting downstream.

The distributions at 75 min further highlight the effect of the H-duct structure. At this stage, the temperature gradient along the main flow direction becomes more distinct in the case without the H-duct, and the local overheating near the windward region is more severe. In comparison, the H-duct case maintains a smoother spatial transition and a more balanced temperature pattern, indicating that the modified inlet organization improves convective heat redistribution during the heating stage.

The results at 160 min correspond to the late holding stage, when the overall field gradually approaches a quasi-steady distribution. Although the temperature difference between the two cases is reduced compared with the heating stage, the H-duct case still exhibits a more uniform temperature field and a less pronounced high-temperature concentration. This result suggests that the benefit of the H-duct structure is not limited to the transient heating period, but also contributes to maintaining thermal uniformity during the subsequent holding stage.

In the later stage of insulation (t = 160 min), as the temperature inside the tank gradually stabilizes, heat transfer within the component continues, and the temperature difference between the two models has decreased. The model with the H-shaped slot shows a relatively uniform overall temperature distribution, with only a small difference remaining at the edges, indicating that a good temperature distribution foundation had already been established during the heating stage. Although the model without the H-shaped slot also shows a reduction in temperature difference, there is still a certain temperature gradient, indicating that the temperature non-uniformity formed in the earlier stage has not been completely eliminated, which may have some impact on subsequent curing uniformity.

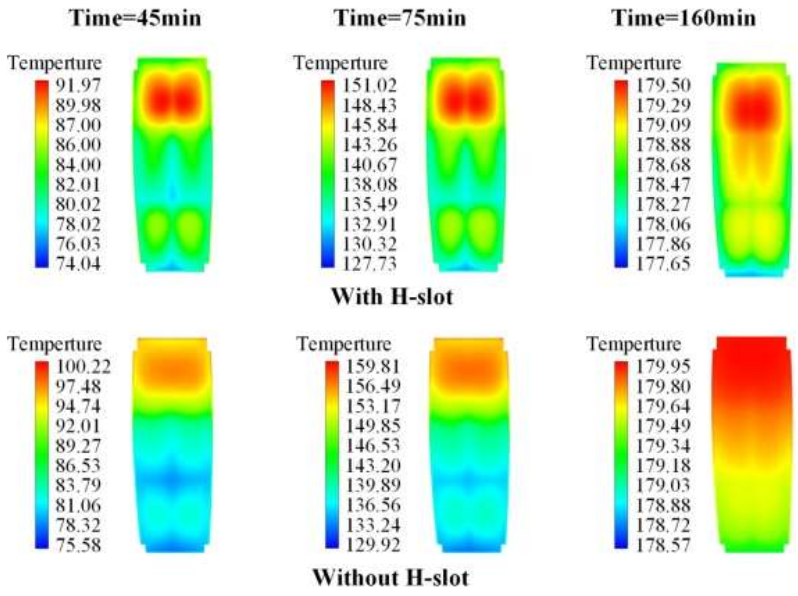


Figure 5 Temperature cloud maps with and without H-shaped grooves at different times

The temperature-difference histories are shown in Fig. 6. The curves indicate that the H-duct structure effectively suppresses the transient temperature non-uniformity during the heating stage, where the largest deviations usually occur. In the case without the H-duct, the temperature difference rises rapidly and reaches a much higher peak, whereas the H-duct case exhibits a lower peak and a smoother subsequent decay. This confirms that the H-duct improves the internal airflow organization and enhances the heat-transfer uniformity of the autoclave system.

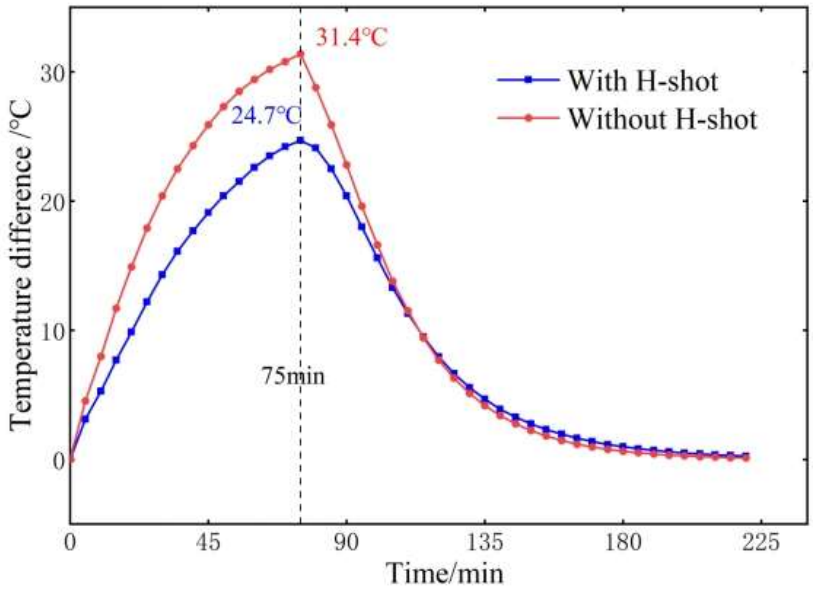


Figure 6 Temperature Difference History With and Without H Slot

Taken together, the results in Figs. 5 and 6 indicate that the H-duct-aware forward model can reproduce the influence of inlet-flow organization on temperature-field evolution more realistically. The improved agreement with experimental observations further supports the use of this forward model as a physically reliable data source for the subsequent rapid-prediction framework.

3.2 Rapid prediction results of temperature field based on MSCGAN

As can be seen from Figure 7, this article standardizes the experimental environment, training parameters, and model implementation details. A dataset was constructed using 100 sets of operating conditions, ultimately obtaining 105,600 training samples and 26,400 validation samples. The training set and validation set are divided according to the operating condition dimension to ensure the rationality of the model generalization ability evaluation. To represent local heat-transfer interactions, the graph topology is constructed using the K-nearest neighbors (KNN) algorithm, and the connectivity remains unchanged throughout the curing cycle. For each node, the four nearest neighbors are selected as the adjacent set. This choice reflects a balance between physical locality and computational efficiency. Since heat conduction is mainly governed by local thermal interactions, each node is primarily influenced by its immediate neighborhood. A smaller $k$may fail to preserve local conduction continuity, whereas a larger $k$may introduce unnecessary nonlocal coupling, blur high-gradient details, and increase graph complexity. Therefore, $k = 4$ is adopted to preserve the essential local heat-transfer topology while maintaining a sparse and efficient graph structure. This graph construction strategy also avoids isolated nodes caused by uneven spatial distribution and preserves consistent local sparsity across different spatial regions.

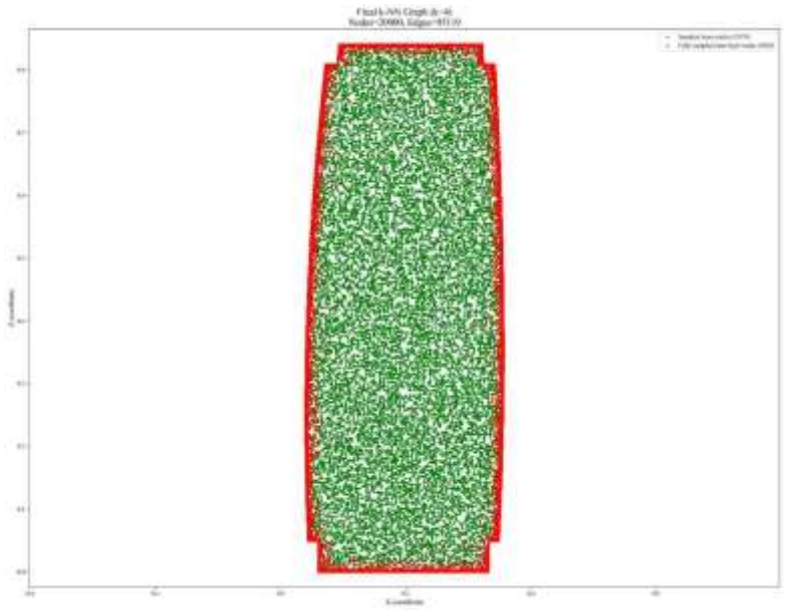


Figure 7 k-NN Graph Construction Results of Temperature Field for Unstructured Grid

The comparison between the ground-truth and predicted temperature fields at representative curing times is shown in Fig. 8. Three instants are selected, namely 2400 s in the first-stage heating period, 4800 s in the second-stage heating period, and 12000 s in the holding stage, to evaluate the ability of MSCGAN to reconstruct the evolving thermal field.

The results at 2400 s indicate that MSCGAN can already capture the main spatial pattern during the rapid-heating stage, including the high-temperature zone near the lower region and the vertical temperature gradient across the component. The corresponding error map remains low over most areas, suggesting that the model can effectively reconstruct the early transient thermal field.

The results at 4800 s show that the model continues to follow the strengthening and outward expansion of the high-temperature region during the second heating stage. At this time, both boundary heat transfer and internal conduction become more influential, yet the predicted contours remain highly consistent with the reference field, indicating that the model can preserve both the global trend and the local gradient distribution.

The results at 12000 s demonstrate that MSCGAN also performs well during the holding stage, when the field evolution becomes slower and approaches a quasi-steady distribution. The predicted temperature field is nearly indistinguishable from the reference field, and the residual error is limited to a few weak local regions, confirming the robustness of the model over the full

curing cycle.

At 12,000 seconds during the insulation stage, the temperature field changes significantly slow down, and overall it approaches a quasi-steady-state distribution. At this time, the model's predicted results are basically consistent with the true values, with very small spatial distribution differences. Error analysis shows that the maximum error at this stage is only 0.23°C, significantly reduced compared to the heating stage, indicating that the model has high prediction accuracy during the insulation stage. Although there is still a slight overall deviation in the error map, the magnitude is small and has basically no impact on the assessment of the temperature field's spatial distribution and the location of high-temperature areas.

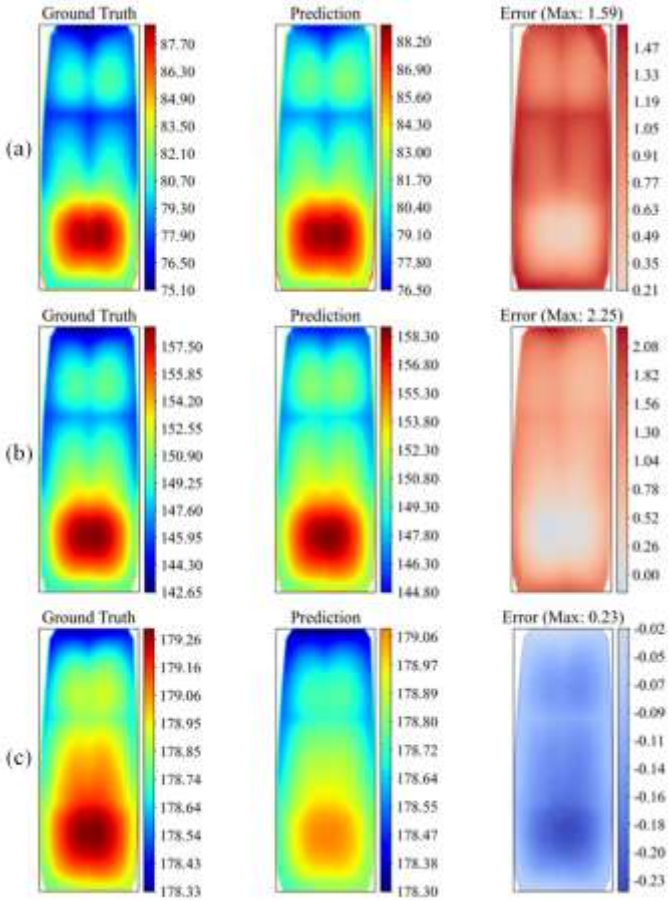


Figure 8 Comparison of MSCGAN model predicted temperature cloud maps at 2400 s, 4800 s, and 12000 s

Figure 9 compares the changes in the maximum, minimum, average, and standard deviation values of the temperature field during the curing process between the actual and predicted values. Overall, the predicted curves maintain a high consistency with the actual curves in terms of evolution trends. In particular, the three types of statistics—maximum, minimum, and average—

can better vary synchronously with the process temperature, reflecting that the established model has strong fitting ability for the overall level of the temperature field and its temporal evolution. As the process temperature gradually increases, the various statistical values of the temperature field show an overall upward trend and gradually stabilize in the later stage. The predicted results essentially reproduce this variation process, indicating that the model can accurately capture the response characteristics of the temperature field during the curing process.

Compared with the maximum, minimum, and average values, the standard deviation better reflects the degree of spatial non-uniformity in the temperature field. As seen from the figure, the standard deviation of the true values shows noticeable peaks in the early-middle and middle-late stages, indicating that the spatial non-uniformity of the temperature field does not change monotonically during the curing process, but instead undergoes a dynamic process of strengthening, weakening, and then strengthening again. The prediction results follow this trend well, with the time intervals of the peaks basically coinciding with those of the true values, though the peak magnitudes are slightly lower than the true curve, suggesting that the model still shows some smoothing in areas with large temperature gradients and drastic local changes. Overall, the model not only maintains good consistency with the global statistical characteristics of the temperature field but also reflects, to a certain extent, the evolution pattern of spatial non-uniformity, meeting the basic requirements for predicting the curing temperature field.

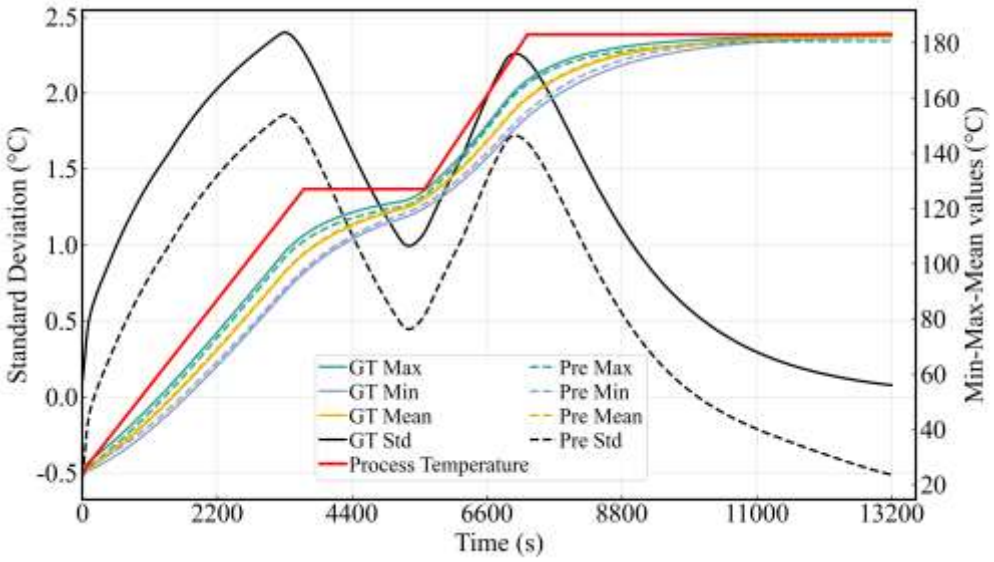


Figure 9 Comparison of statistical characteristics of temperature fields between true values and predicted values

Figure 10 shows the MAPE distribution of the original samples, mean statistics, minimum statistics, and maximum statistics under four working conditions. Overall, the error distribution of the original samples and mean statistics is relatively concentrated. The medians of the four working conditions are mostly around 0.20, with the medians of Case 1, Case 3, and Case 4 basically in the 0.20-0.22% range, and Case 2 slightly higher, close to 0.23%. This indicates that the model's predictions for the overall level of the temperature field are relatively stable, with relatively limited differences between different working conditions.

In comparison, the error distributions of the minimum and maximum statistics are generally shifted upward. As shown in Figure 10(c), the medians of Case 3 and Case 4 in the minimum statistics are roughly between 0.27-0.30%, while Case 1 is about 0.33%, and Case 2 is close to 0.38%; in Figure 10(d), the differences in the maximum statistics are more pronounced, with the medians of Case 3 and Case 4 around 0.26-0.29, Case 1 about 0.36%, and Case 2 the highest, nearly 0.43%. Meanwhile, in both the minimum and maximum statistics, Case 2 has wider boxes, longer upper whiskers, and more outliers, with some sample errors approaching 0.8-0.9%, indicating that under this operating condition, the model's prediction fluctuates more for extreme value features.

From a lateral comparison of different operating conditions, Case 3 generally has lower box positions across the four types of indicators and a more concentrated distribution, indicating relatively the best prediction stability; Case 4 is close to Case 3, but slightly higher in minimum and maximum value statistics; Case 1 is overall at a medium level; Case 2 shows higher error levels in all four types of indicators, especially more noticeable in extreme value statistics. Overall, the model performs better in predicting original samples and mean statistics than in minimum and maximum statistics, fitting the overall characteristics of the temperature field well. In addition, compared to traditional numerical models, the proposed model can complete predictions within 42 seconds under different operating conditions, while the numerical model requires 7038 seconds, reducing computation time by approximately 99.4%, significantly improving computational efficiency while maintaining prediction accuracy.

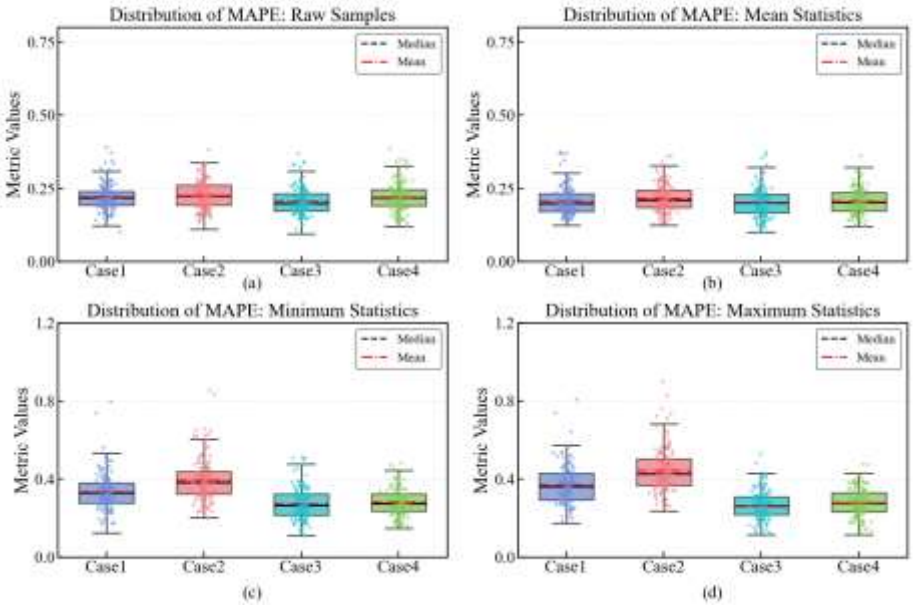


Figure 10 MAPE distribution of original samples, mean statistics, minimum statistics, and maximum statistics under four operating conditions

Figure 11 shows the error variation results of different models in full-process autoregressive prediction tasks. Compared with single-step prediction, autoregressive prediction better reflects the error propagation and accumulation characteristics of the model in long-term rolling inference. The results indicate that MSCGAN's MAPE remains below 0.81% throughout the entire period, and it can still maintain a low error level during rapid temperature changes, suggesting that the model is not only capable of achieving high-precision mapping from the current state to the temperature field at the next moment, but also effectively suppresses error diffusion in long-term recursive predictions.

From the initial curing stage to the end of the first heating phase, all model errors remain low, but the error growth of MSCGAN is the slowest. This indicates that the model can predict the temperature field at the next moment relatively stably using the current state information in the initial stage, and effectively mitigates the accumulation effect of single-step deviations in the continuous rolling process. As the process enters the stage of rapid temperature change, the errors of all models rise to varying degrees, indicating that the heating phase is the most challenging stage for the entire process prediction. The main reason is that the temperature field evolves quickly during this stage, and local gradients are enhanced, so any single-step prediction deviation will be further amplified in subsequent recursions. Nevertheless, the peak error of MSCGAN is still significantly lower than that of other models, indicating that it has a stronger capability to

model the dynamic evolution of the temperature field during non-stationary stages.

Near the warming stage of the second phase, errors of all models rose again, but the increase in MSCGAN remained the smallest, and its overall fluctuations were also more stable. This result indicates that the multi-scale graph generator and local adversarial discriminator not only improve single-step prediction accuracy, but more importantly, enhance the model's ability to control local structural distortion and boundary blurring during long-term sequential inference. In contrast, ordinary GNNs, Graph U-Nets, and regular grid GAN models are more prone to sustained error accumulation during multi-step rolling predictions, which is related to their insufficient representation of multi-scale heat diffusion relationships and local high-gradient regions.

During the insulation phase, as the temperature field evolution tends to stabilize, the errors of all models decrease and enter a relatively stable state, but MSCGAN consistently maintains the lowest error level. This indicates that the model does not exhibit significant drift at the end of the full-process prediction due to the accumulation of early-stage errors, but is able to continue maintaining high accuracy in the later stage.

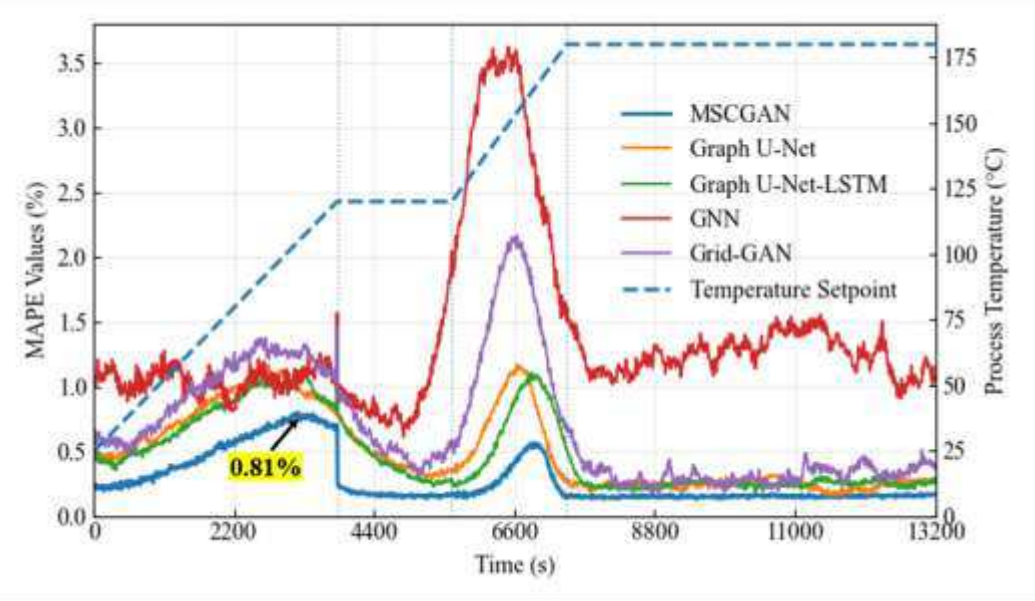


Figure 11 Comparison of Autoregressive Prediction Results

3.3 Model comparison analysis and ablation experiment

Table 2 presents the quantitative comparison results of different models in the task of predicting curing temperature fields. It can be seen that MSCGAN achieves the best results across all evaluation metrics, with an MAE and RMSE of 1.28 and 1.76, respectively, an R^2 of 0.993,

and a maximum error of 3.58. This indicates that the model performs well in overall error control, fitting the temperature variation trends, and predicting local extreme regions.

Further comparison shows that the prediction results of GraphU-Net and GraphU-Net-LSTM are relatively close, but their overall performance is still lower than MSCGAN. Compared with GraphU-Net, MSCGAN's MAE decreased from 1.87 to 1.28, RMSE decreased from 2.58 to 1.76, and maximum error decreased from 7.22 to 3.58; compared with GraphU-Net-LSTM, MAE decreased from 1.67 to 1.28, RMSE decreased from 2.39 to 1.76, and maximum error decreased from 7.95 to 3.58. This indicates that merely using a graph encoder-decoder structure, or introducing temporal modeling on this basis, while able to improve prediction accuracy, still has shortcomings in controlling errors in complex and extreme regions. In contrast, MSCGAN demonstrates a better balance between overall accuracy and local error control.

From the results of the other two models, Grid-GAN has an MAE and RMSE of 2.46 and 3.35, respectively, an R^2 of 0.976, and a maximum error of 8.37, with the overall error further increasing; the traditional GNN performs the worst, with an MAE and RMSE of 4.96 and 6.33, an R^2 of only 0.916, and a maximum error reaching 14.81. It can be seen that when the model's ability to represent the spatial correlation and dynamic variation features of the temperature field decreases, all error metrics worsen significantly, especially the maximum error, which increases more prominently.

Overall, for problems like the curing temperature field that have both spatial heterogeneity and temporal evolution characteristics, it is difficult to achieve ideal prediction results by relying solely on basic graph structure modeling or regular grid generation methods. MSCGAN not only ensures overall prediction accuracy but also effectively reduces errors in local extreme regions, thus possessing stronger representation capability for the spatial distribution of the temperature field and its dynamic evolution process.

Table 2 Comparison of Prediction Performance of Different Models

Model	MAE / ℃	RMSE / ℃	R^2	MAX-Error / ℃
MSCGAN	1.28	1.76	0.993	3.58
Graph U-Net	1.87	2.58	0.982	7.22
Graph U-Net-LSTM	1.67	2.39	0.984	7.95
Grid-GAN	2.46	3.35	0.976	8.37
GNN	4.96	6.33	0.916	14.81

Table 3 presents the ablation experiment results of MSCGAN and its various variant models, used to analyze the impact of the adversarial learning mechanism, CLJP module, skip connections, and discriminator structure on the prediction performance of the curing temperature field. Overall, the complete model MSCGAN achieved the best results across all four metrics, with MAE, RMSE, R^2, and MAX-Error being 1.28, 1.76, 0.993, and 3.58, respectively, indicating that under the joint effect of all components, the model performs well in overall accuracy, fitting ability, and local error control.

From the results of removing the adversarial learning mechanism, Noadv's MAE and RMSE increased to 2.05 and 2.88, respectively, R^2 decreased to 0.952, and the maximum error increased to 11.80, showing a significant performance decline. This indicates that the adversarial learning mechanism plays an important role in improving the realism and stability of prediction results, especially contributing significantly to controlling local large errors. Without the adversarial constraint, although the model can still learn the basic variation patterns of the temperature field, its ability to depict complex regions and extreme value areas is significantly weakened.

After removing the CLJP module, the model error also increased significantly, with MAE and RMSE rising to 1.72 and 2.41 respectively, R^2 dropping to 0.963, and MAX-Error reaching 9.43. Compared with the complete model, NoCLJP shows degradation across all metrics, indicating that the CLJP module plays an important role in enhancing the model's feature representation capability. The introduction of this module helps to strengthen the model's ability to extract complex spatial correlation features of the temperature field, thereby improving overall prediction performance and reducing error levels in local regions.

The performance of the NoSkip model declines most significantly, with its MAE and RMSE reaching 2.41 and 3.45, respectively, R^2 dropping to 0.938, and the maximum error increasing to 14.21, making it the worst among all ablated models. This indicates that skip connections play an irreplaceable role in the model. On one hand, skip connections can preserve shallow feature information and prevent feature loss during multi-layer propagation; on the other hand, they are also important for restoring local details and boundary information in the temperature field. Without this structure, the model's ability to jointly model global information and local details is significantly weakened, resulting in the most noticeable increase in error.

For the GlobaD model, its MAE, RMSE, and MAX-Error are 1.65, 2.32, and 6.76,

respectively. Although the overall performance is still better than Noadv and NoSkip, there is still a significant gap compared to the complete model. This indicates that while the global discriminator can improve the overall consistency of generated results to some extent, compared with the discrimination method used in MSCGAN, its ability to constrain local details and complex regions is still limited, and it is therefore inferior to the complete model in terms of maximum error control and overall accuracy.

As shown in Table 3, all component modules have a positive effect on improving model performance, but the degree of impact varies. Among them, skip connections and the adversarial learning mechanism have the most significant influence on model performance, while the CLJP module and the optimization of the discriminator structure also play an important role in improving prediction accuracy. The complete model outperforms all ablation variants across the four metrics, indicating good synergy among the modules, jointly ensuring the model effectively represents the spatial distribution characteristics of the curing temperature field and its dynamic evolution patterns.

Table 3 MSCGAN Ablation Experiment Results

Model	MAE / ℃	RMSE / ℃	R^2	MAX-Error / ℃
MSCGAN	1.28	1.76	0.993	3.58
Noadv	2.05	2.88	0.952	11.80
NoCLJP	1.72	2.41	0.963	9.43
NoSkip	2.41	3.45	0.938	14.21
GlobalD	1.65	2.32	0.973	6.76

4. Conclusion

(1) This paper proposes a high-fidelity data generation method of an autoclave curing process considering the H-grove duct structure, and completes multi-condition transient simulation, parameter sampling, and sample construction based on the thermo-chemical coupling pre-model of the autoclave. The results show that this process can provide a unified and reliable data foundation for rapid prediction models and lay a sample foundation for subsequent rapid prediction of the temperature field in non-structural grids.

(2) Compared with traditional single-scale graph networks, regular grid GANs, and other comparison models, the MSCGAN model proposed in this paper demonstrates superior accuracy and stability when predicting the curing temperature field of an autoclave under non-structured grids. Quantitative results show that the model achieves a MAE as low as 1.28°C, an RMSE of

1.76°C, an R^2 of 0.993, and a maximum error of only 3.58°C. It can accurately reproduce the temperature field distribution throughout the entire heating and holding stages, with the evolution of statistical features highly consistent with the true values, and the autoregressive prediction MAPE always remaining below 0.81%.

(3) MSCGAN, through the collaborative design of two-level CLJP coarsening, graph attention networks, skip connections, and local graph discriminators, effectively addresses the issues of insufficient multi-scale feature representation and over-smoothing prediction on unstructured meshes. The coarsening module enlarges the receptive field to capture global heat diffusion relationships, the attention mechanism adaptively aggregates key neighborhood information, skip connections preserve fine-scale boundaries and high-gradient details, and the local discriminator suppresses blurring and distortion in the temperature field, achieving cooperative representation of global trends and local details.

Declarations

a.Funding

This work was supported by the National Engineering and Research Center for Commercial Aircraft Manufacturing under Grant No. COMAC-SFGS-2022-1875.

b.Conflict of interest / Competing interests

No conflict of interest.

c.Authors' contributions

Guangqi Qiu: Conceptualization, research framework design, and writing – review and editing.

Yongqian Xu: Conceptualization, supervision, project administration, and funding acquisition.

Peng Huang: Supervision and methodology.

Yingkui Gu: Supervision and resources.

Wenjing Yu: Methodology, experimental design, formal analysis, and writing – original draft.

Ning Zhong: Methodology, data analysis, model calculation, and writing – original draft.

References

[1] Dolkun D, Wang H, Wang H, et al. Influence of large framed mold placement in autoclave on heating performance[J]. Applied Composite Materials, 2020, 27(6): 811-837.

[2] Han N, An L, Fan L, et al. Research on temperature field distribution in a frame mold during autoclave process[J]. Materials, 2020, 13(18): 4020.

[3] Zhang G, Zhang B, Luo L, et al. Influence of mold and heat transfer fluid materials on the temperature distribution of large framed molds in autoclave process[J]. Materials, 2021, 14(15): 4311.

[4] Sun Y, Gao D, Zhang Z, et al. Research on air-flow-field characteristics and structural optimization of the guide channels of the autoclave[J]. Energies, 2022, 15(3): 1119.

[5] Yue B, Xu Y, Zhang W. A novel topology optimization of the frame mold for composite autoclave process[J]. Applied Composite Materials, 2022, 29(6): 2343-2365.

[6] Yue B, Xu Y, Teng X, et al. A novel thermal-fluid topology optimization of the frame mold for composite autoclave process[J]. Applied Thermal Engineering, 2024, 247: 123050.

[7] Xu Y, Zhan L. Simulation investigation of temperature distribution in large aluminium panel during autoclave age forming process[J]. International Journal of Computational Materials Science and Surface Engineering, 2018, 7(3/4): 169.

[8] Bohne T, Frerich T, Jendrny J, et al. Simulation and validation of air flow and heat transfer in an autoclave process for definition of thermal boundary conditions during curing of composite parts[J]. Journal of Composite Materials, 2018, 52(12): 1677-1687.

[9] Weber T A, Arent J C, Münch L, et al. A fast method for the generation of boundary conditions for thermal autoclave simulation[J]. Composites Part A: Applied Science and Manufacturing, 2016, 88: 216-225.

[10] Fisher A, Levy A, Kratz J. Effects of heat transfer coefficient variations on composite curing[J]. Journal of Composite Materials, 2023, 57(3): 363-376.

[11] Wang L, Zhu W, Wang Q, et al. A heat-balance method for autoclave process of composite manufacturing[J]. Journal of Composite Materials, 2019, 53(5): 641-652.

[12] Zhu J, Frerich T, Dimassi A, et al. Experimental validation of a quasi-transient coupling approach for the modeling of heat transfer in autoclave processing[J]. Journal of Composite Materials, 2022, 56(5): 797-810.

[13] Zhu J, Frerich T, Dimassi A, et al. A quasi-transient coupling approach to the modeling of conjugate heat transfer in the autoclave[J]. Journal of Reinforced Plastics and Composites, 2021, 40(23-24): 912-926.

[14] Yang Z, Liu L, Li D. Full Coupling Modeling on Multi-Physical and Thermal–Fluid–Solid Problems in Composite Autoclave Curing Process[J]. Materials, 2025, 18(7): 1471.

[15] Lin Y, Guan Z. The use of machine learning for the prediction of the uniformity of the degree of cure of a composite in an autoclave[J]. Aerospace, 2021, 8(5): 130.

[16] Hou J, You B, Xu J, et al. Prediction of curing process for thermosetting prepreg compression molding process based on machine learning[J]. Polymer Composites, 2022, 43(3): 1749-1762.

[17] Kyriazi E, Petsinis G, Zervos C, et al. ML-based surrogate cure simulation for predicting process time and temperature overshoot in resin transfer moulding[J]. Journal of Reinforced Plastics and Composites, 2025: 07316844251390926.

[18] Feng G, Liu B. Probability Prediction of Curing Process-Induced Deformation for V-Shape Composite Structures Based on FEM Method and Data Mining[J]. Materials, 2024, 17(14): 3545.

[19] Yang S, Yao W, Zhu L F, et al. Predicting the temperature field of composite materials under a heat source using deep learning[J]. Composite Structures, 2023, 321: 117320.

[20] Zhang R, Liu Y, Zheng T, et al. A fast spatio-temporal temperature predictor for vacuum assisted resin infusion molding process based on deep machine learning modeling[J]. Journal of Intelligent Manufacturing, 2024, 35(4): 1737-1764.

[21] Wu Y, Cao Z L, Liu C, et al. Temperature field and curing degree prediction of large composite blades based on coupled finite element analysis and machine learning[J]. Polymer Composites, 2025, 46(S1): S621-S637.

[22] Zhang Y, Gong Z, Zhou W, et al. Multi-fidelity surrogate modeling for temperature field prediction using deep convolution neural network[J]. Engineering Applications of Artificial Intelligence, 2023, 123: 106354.

[23] Liu Q Q, Liu S T, Li Y G, et al. Non-contact and full-field online monitoring of curing temperature during the in-situ heating process based on deep learning[J]. Advances in Manufacturing, 2024, 12(1): 167-176.

[24] Raissi M, Perdikaris P, Karniadakis G E. Physics-informed neural networks: a deep learning framework for solving forward and inverse problems involving nonlinear partial differential equations[J]. Journal of Computational Physics, 2019, 378: 686-707.

[25] Amini Niaki S, Haghighat E, Campbell T, et al. Physics-informed neural network for modelling the thermochemical curing process of composite-tool systems during manufacture[J]. Computer Methods in Applied Mechanics and Engineering, 2021, 384: 113959.

[26] Meng Q, Li Y, Liu X, et al. A novel physics-informed neural operator for thermochemical curing analysis of carbon-fibre-reinforced thermosetting composites[J]. Composite Structures, 2023, 321: 117197.

[27] Lu L, Jin P, Pang G, et al. Learning nonlinear operators via DeepONet based on the universal approximation theorem of operators[J]. Nature machine intelligence, 2021, 3(3): 218-229.

[28] Zhao Z, Liu C, Li Y, et al. Diffeomorphism neural operator for various domains and parameters of partial differential equations[J]. Communications Physics, 2025, 8(1): 15.

[29] Li Z, Zheng H, Kovachki N, et al. Physics-informed neural operator for learning partial differential equations[J]. ACM / IMS J. DATA Sci., 2024, 1(3): 9:1-9:27.

[30] Kovachki N, Li Z, Liu B, et al. Neural operator: learning maps between function spaces with applications to PDEs[J]. Journal of Machine Learning Research, 2023, 24(89): 1-97.

[31] Patel J M, Ramezankhani M, Deodhar A, et al. An extended physics-informed neural operator for accelerated design optimization in composites autoclave processing[J]. Composites Part B: Engineering,

2026, 308: 112935.

[32] Zhou J, Cui G, Hu S, et al. Graph neural networks: A review of methods and applications[J]. AI open, 2020, 1: 57-81.

[33] Würth T, Freymuth N, Zimmerling C, et al. Physics-informed MeshGraphNets (PI-MGNs): Neural finite element solvers for non-stationary and nonlinear simulations on arbitrary meshes[J]. Computer Methods in Applied Mechanics and Engineering, 2024, 429: 117102.

[34] Grattarola D, Zambon D, Bianchi F M, et al. Understanding pooling in graph neural networks[J]. IEEE transactions on neural networks and learning systems, 2022, 35(2): 2708-2718.

[35] Li Z P, Wang S G, Zhang Q H, et al. Graph pooling for graph-level representation learning: a survey[J]. Artificial Intelligence Review, 2024, 58(2): 45.